

The formation of astrophysical Mg-rich silicate dust

Christopher M. Mauney^{a,1}, Davide Lazzati^{b,1}

^a*mauneyc@oregonstate.edu*

^b*lazzatid@science.oregonstate.edu*

Abstract

We present new results for ground-state candidate energies of Mg-rich olivine (MRO) clusters and use the binding energies of these clusters to determine their nucleation rates in stellar outflows, with particular interest in the environments of core-collapse supernovae (CCSNe). Low-lying structures of clusters $(\text{Mg}_2\text{SiO}_4)_n$ $2 \leq n \leq 13$ are determined from a modified minima hopping algorithm using an empirical silicate potential in the Buckingham form. These configurations are further refined and optimized using the density functional theory code Quantum Espresso. Utilizing atomistic nucleation theory, we determine the critical size and nucleation rates of these clusters. We find that configurations and binding energies in this regime are very dissimilar from those of the bulk lattice. Clusters grow with SiO_4 -MgO layering and exhibit only global, rather than local, symmetries. When compared to classical nucleation theory we find suppressed nucleation rates at most temperatures and pressures, with enhanced nucleation rates at very large pressures. This implies a slower progression of silicate dust formation in stellar environments than previously assumed.

1. Introduction

Cosmic dust presents an intriguing laboratory to the physicist. The cycle of dust, its crucial role in a great galactic recycling and processing of material, necessitates a broad view. Yet any approach to the study of dust that does not incorporate the details of small-scale chemistry and kinetics, up to and including quantum effects, will fail as a predictive model. This is

¹Oregon State University

especially true when examining dust formation, when the physics is in the most dynamic phase of the cycle.

Silicate dust is a major component of dust present in the ISM. Absorption features at $9.7 \mu\text{ m}$ and $18 \mu\text{ m}$ are associated with the Si-O stretching and O-Si-O bending modes in silicates [1]. Similar spectral features have been observed in other galaxies [2, 3]. These lines are strong and broad, indicating that in the diffuse ISM silicates are structurally amorphous [4]. However, crystalline silicate features have been observed around AGB stars and stars with disks [5, 6], and in comets [7]. These observations indicate that a substantial fraction of silicate dust grains are in a crystal structure before being injected into the ISM. It is possible that crystallization occurs directly from the vapor, and subsequent processing by grain-grain collisions, shock sputtering, and thermal annealing leads to amorphization [8]. However, the reverse is also possible, where amorphous silicate is formed from the vapor and later processed into crystalline structure.

Determining the formation pathway of silicate dust grains is necessary for making more accurate predictions of dust properties. In this paper we continue the approach set forth in our previous paper on carbon dust precursors [9] with the Mg-rich olivine (MRO) clusters $(\text{Mg}_2\text{SiO}_4)_n$, for $2 < n < 13$. In principle, to exactly determine nucleation of multi-species molecules, all pathways through a high-dimensional Gibbs energy surface are necessary. For the reasons given in the next section, we instead follow a fixed stoichiometric ratio into larger molecules.

This paper is organized as follows: in section 2 we detail our methods for cluster ground state configuration and density functional theory energy calculations. Results of these calculations are presented in section 3, showing binding energies of clusters, critical sizes, and nucleation rates. We summarize these results and discuss their impact in section 4.

2. Methods

2.1. Selecting the nucleation pathway

In principle the formation pathway of silicates can take many directions through precursor molecules that do not necessarily maintain a fixed stoichiometry. It is to be expected, however, that the stoichiometry of the precursor molecule will eventually approach the one of the crystal. Since it is computationally impractical to compute the properties of all possible precursor molecules, in this study we only investigate molecules of the form

$(\text{Mg}_2\text{SiO}_4)_n$. While this is a limitation of this work, it is worth noting that it is still a significant improvement over the capillary approximation used in other investigations of silicate nucleation (see, e.g., [10, 11]). Not only the fixed stoichiometry is implicitly assumed, but also the precursor molecules are taken to be spherical and possessing the physical properties - such as surface energy - of the bulk material. While some studies [12, 13] have attempted a full study of precursor molecules of free stoichiometry, they were limited to small molecules ($n < 10$) (the larger molecules in those studies did follow fixed stoichiometries).

2.2. Determining ground state configuration

A molecular configuration approximating the ground state of the molecule must be supplied to the DFT calculation. We use an implementation of the global minima search algorithm minima-hopping (MH) developed by Goedecker [14]. Minima hopping does not generate new configurations based on random moves, as other global minima techniques such as basin hopping, but rather smoothly follows the energy surface by applying molecular dynamics to the system. Starting from an initial state, the system is given a kinetic energy and allowed to evolve according to the equations of motion. The stopping criterion of the molecular dynamics algorithm is passing over one or two hills on the potential energy surface (that is, the system goes over from increasing to decreasing energy).

New configurations are subjected to a minimization after the molecular dynamics step. The minimized configuration is compared to the previous (beginning) one. If the two configurations are determined to be the same (in this case, comparing inter-atomic distances of atoms), the algorithm returns to performing the molecular dynamics step with the an increased kinetic energy. If the system escapes the current energy well into a new unique one (that is, a new configuration is found), the kinetic energy is reduced, and the process is started again. Details on the specifics of implementation of the algorithm can be found in [14]. All the parameters we used in this article can be found in Table 4.

We use a modified version of minima hopping that implements an atom-swap. This algorithm defines a small (1-5%) probability α that the next cycle will swap positions of two randomly selected atoms in the molecule rather than do a molecular dynamics run. This use of non-local transformations has been applied to basin-hopping and has been found to increase the efficiency of such searches [15]. In our approach, a temperature T_s is used in a

Table 1. Charges of elements

atom	charge (e)
Mg	+2.0
O	-2.0
Si	+4.0

simple Metropolis condition $\exp(-\Delta E/T_s)$ after the swap to determine if the swapped positions should be accepted as the new state of the search, where ΔE represents the relative change in energy.

The potential function used in this study is the Bees-Kramer-van Santen (BKS) model [16]. The functional form is given as a combination of Coulomb and Buckingham potential terms

$$\begin{aligned}
 U(\mathbf{r}) &= \sum_{i<j} U_{ij} + \sum_{i<j<k} U_{ijk} \\
 U_{ij} &= \frac{q_i q_j}{r_{ij}} + A_{ij} \exp(-r_{ij}/B_{ij}) - C_{ij} r_{ij}^{-6} \\
 U_{ijk} &= K_{ijk} (\theta_{ijk} - \theta_{0,ijk})^2
 \end{aligned} \tag{1}$$

where the variable r_{ij} is the inter-atomic distance between atoms i and j and q_i is the charge on atom i . The pair-wise parameters A_{ij} and B_{ij} specify a short range repulsive force and C_{ij} a long range attractive force. The three-body parameter K_{ijk} is a force constant, θ_{ijk} is the angle formed from atoms i, j, k , and θ_0 is the equilibrium angle. Values for these parameters are determined from ab-initio studies and reliably reproduce the properties of crystalline and large amorphous silicates. The values used in this study are given in Tables 1, 2, & 3 [17, 18, 19].

Table 4 gives the values used for our minima hopping parameters. Verlet integration is used to evolve the system during the molecular dynamics step of the minima hopping algorithm. A Broyden-Fletcher-Goldfarb-Shanno (BFGS) [20] algorithm is used for the minimization step.

Our atom-swap method results in most cases in faster searches. Figure 1 shows a comparison between traditional minima hopping and minima hop-

Table 2. Pair-potential parameters for the Buckingham potential

pair	$A_{ij}(eV)$	$B_{ij}(\text{\AA}^{-1})$	$C_{ij}(eV\text{\AA}^{-6})$
O-O	22764.0	1/0.149	27.88
Si-O	1283.907	1/0.32052	10.66158
Si-Si	79502.113	1/0.201	446.780
Mg-O	821.6	1/0.3242	0.0

Table 3. Three-body potential parameters

tuple	$K_{ijk}(eV\text{\AA}^{-2})$	$\theta_{0,ijk}$
O-Si-O	2.097	109.47°
O-Mg-O	2.097	90.0°

Table 4. Minima hopping parameters

α_1	α_2	β_1	β_2	β_3	$E_{diff}^0(eV)$	$T_0(K)$
0.95	1.05	1.05	1.05	0.95	0.5	1000

ping with atom-swap for a $n = 4$ and $n = 6$ test case. In both cases, the atom-swap method yields lower energies. Figure 2 compares atom-swap algorithms with different parameters. The algorithm is not very dependent on the selection of parameters, but appears to work best at $\alpha = 5\%$ and $T = 300$. We select these values for this article.

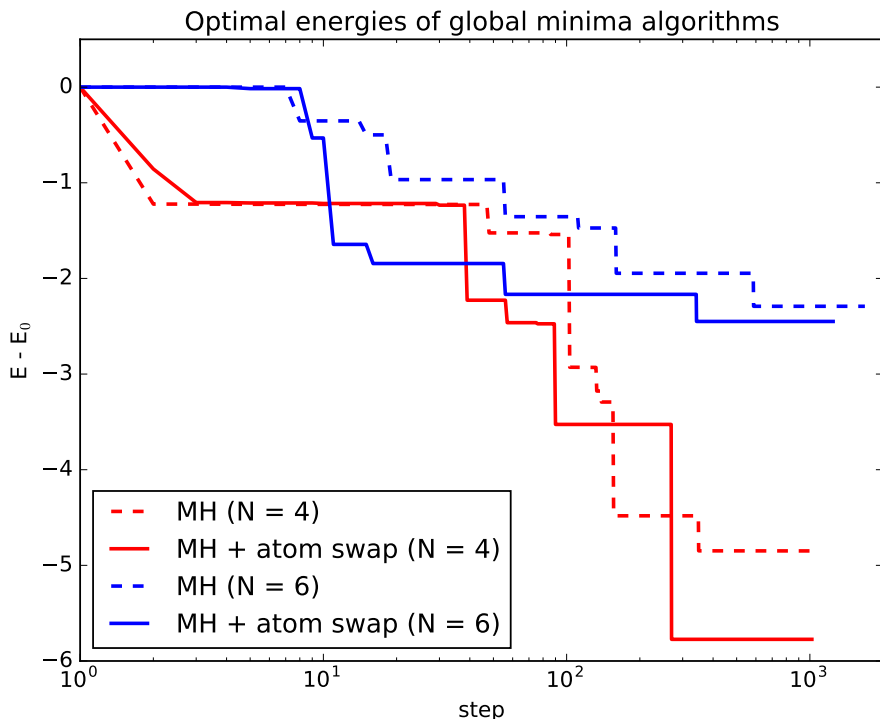


Figure 1 Performance of traditional minima-hopping algorithms (dashed) compared with minima-hopping with atom-swap included (solid), using the same initial starting configuration.

The number of discoverable minima increases exponentially with the size of the molecule. It is therefore advantageous, especially for larger silicate clusters, to precondition the input to the minima-hopping algorithm. For larger molecules ($n > 5$), we borrow techniques from genetic algorithms used in structure prediction [21], where previously determined clusters can act as sub-units in the seeds of larger clusters. Inputs are constructed as combinations of smaller molecules found in previous runs. An example is

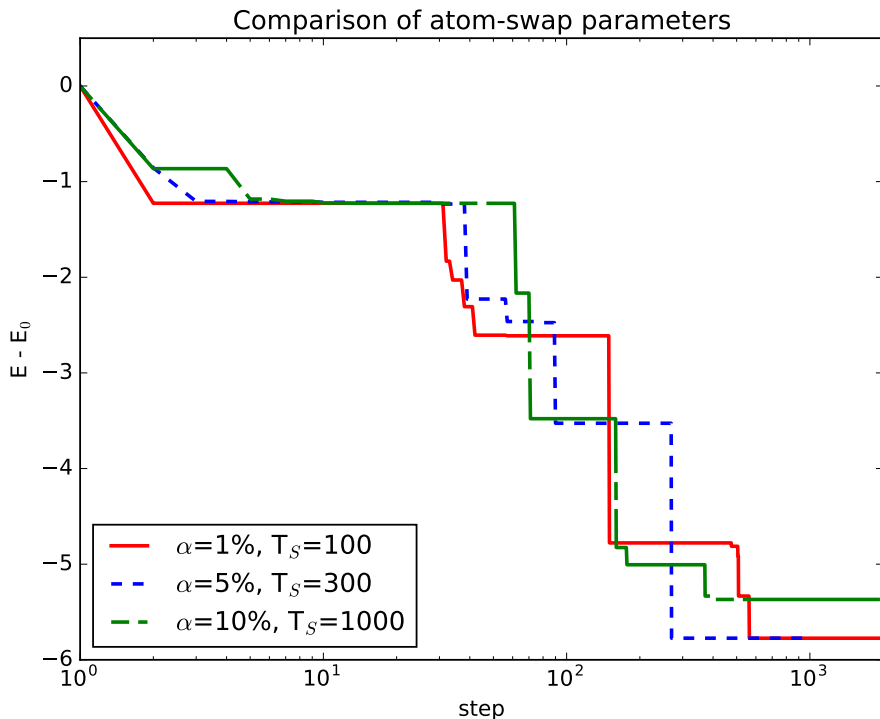


Figure 2 Comparison of different atom-swap parameters (swap % and swap temperature) for the same initial starting configuration.

provided in Figure 3, where we use the optimized state of $(\text{Mg}_2\text{SiO}_4)_3$ to generate the initial search state of the $(\text{Mg}_2\text{SiO}_4)_6$ molecule.

It is possible that the lowest-lying state produced using an empirical potential will not be the lowest in the DFT calculation. To address this, we select 8 lowest-lying candidate configurations from the global search. These are screened using a low-resolution DFT relaxation, and the candidate with the lowest reported energy is selected for a full DFT calculation.

Many of our larger $(\text{Mg}_2\text{SiO}_4)_n$ molecules appear amorphous and lack clear symmetries. The potential given by Eq.(1) can be dominated by electrostatic forces between the Mg^{2+} anions and SiO_4^{4-} cations, limiting the manifestation of large-scale symmetries arising from chemical bonding. However, the thoroughness of our search and robustness of the MH algorithm gives us confidence that our configurations are energetically low-lying states.

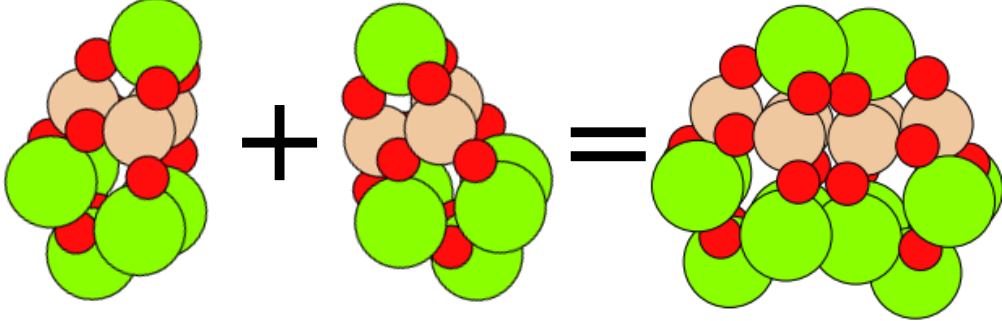


Figure 3 Example procedure of generating starting configurations of larger cluster searches.

2.3. Quantum chemistry calculations of $(Mg_2SiO_4)_n$ clusters

We use the DFT software Quantum ESPRESSO v5.3 (QE) [22] to calculate the binding energies of the $(Mg_2SiO_4)_n$ clusters. What follows is an overview of DFT and the plane-wave approach of QE uses to solve the coupled Kohn-Sham (KS) equations. For a more thorough exploration of the theory, we refer the reader to [9, 23]. An initial guess of the many-body electron density $n(\{\mathbf{r}_i\})$, as a function of the electron positions $\{\mathbf{r}_i\} = (\mathbf{r}_1, \mathbf{r}_2, \dots, \mathbf{r}_N)$, is made and is used to construct an effective potential $V_{eff}([n])$. An updated density $n'(\{\mathbf{r}_i\})$ is found by solving the Kohn-Sham eigenvalue equations

$$\left[\frac{-\hbar^2}{2m_e} \nabla_i^2 + V_{eff} \right] \phi_i = \epsilon_i \phi_i \quad (2)$$

where \hbar is Planks reduced constant, m_e is the electron mass, ϕ_i are the KS orbital basis functions and ϵ_i are the eigenvalues. The new density is recovered as

$$n'(\{\mathbf{r}_i\}) = \sum_i |\phi_i|^2 \quad (3)$$

This iterative procedure is done until self-consistency is achieved, that is when $|n - n'| \leq \delta$, with δ a convergence parameter close to zero. We will be subjecting our clusters to local minimization using BFGS, which can be very computationally expensive. Therefore we set $\delta = 10^{-6}$ to allow for an efficient minimization and still maintain good accuracy of the energy.

The binding energy E_b is given as

$$E_b = E_t - nE_1 \quad (4)$$

where E_t is the total energy and E_1 is the single monomer total energy. The difference represents all energy released from the system following cluster formation.

2.4. Free energy and nucleation

To calculate nucleation rates, we first need to determine the change in free energy when clusters grow. We can construct the free energy of a cluster of size n as

$$G(n) = G_V(n) + G_S(n) \quad (5)$$

where $G_V(n)$ is referred to as the volume term, and $G_S(n)$ as the surface term. These represent, respectively, the energy release when moving vapor monomers to the new phase, and the energy barrier necessary to overcome when doing so. The volume term comes from familiar thermodynamics

$$G_V(n) = -nkT \ln S \quad (6)$$

with supersaturation ratio (hereafter saturation) $S = p/p_e$ where p_e represents the equilibrium pressure, and temperature T . Following [24], we take the pressure as the partial pressure of the key species in the formation of the clusters. The key species represents the constituent element of the vapor with the lowest collision rate, and to good approximation the rate of nucleation is controlled by the density of the key species. For MRO nucleation in astrophysical conditions we find Mg to be the limiting element, in most cases. The equilibrium pressure is given as function of temperature T as

$$\ln(p_e) = -A/T + B \quad (7)$$

where A, B are fitted thermodynamic constants. We use the values by [11], $A = 18.62 \times 10^4 K$ and $B = 52.4336$.

In the classical case of CNT, the capillary approximation is used to represent the surface term. In the atomistic case, we use

$$G_S(n) = \lambda n - E_n \quad (8)$$

where E_n is the binding energy of a cluster of size n and λn represents the binding energy of n monomers in the *bulk* solid phase (e.g. the infinite lattice).

For a full atomistic formulation, we go from n continuous to n discrete, and from Eq. (5-8) construct the work of cluster formation W_n

$$W_n = -nkT \ln S - (E_n - \lambda n) \quad (9)$$

The maximum value of W_n represents the critical cluster size; values at the critical size are denoted with a *, so that the critical size is n^* , the WCF is W^* , ect. To very good approximation the stationary nucleation rate J_s is only a function of critical values

$$J_s = z f^* C^* \quad (10)$$

where z is the Zel'dovich factor, f^* is the attachment rate onto critical clusters and C^* is the concentration of critical clusters. The Zel'dovich factor accounts for the possibility that critical clusters will spontaneously lose a monomer and decay into smaller clusters, rather than grow into the new phase. For the purposes of this work we take $z = 1$ (that is, all critical clusters will grow into the new phase).

2.5. Determination of E_1 and λ

The properties of the molecule $(\text{Mg}_2\text{SiO}_4)_1$, particularly the binding energy E_1 and the bulk lattice cohesive energy λ of a forsterite lattice with respect to $(\text{Mg}_2\text{SiO}_4)_1$, are necessary for our calculations. There exists robust literature on the chemistry of forsterite crystals, but little of it explores possible values of E_1 and there is disagreement on the value λ .

To determine the structure of E_1 , we take a single $(\text{Mg}_2\text{SiO}_4)_1$ from the bulk lattice consisting of the octahedral sites M1, M2, and the SiO_4 belonging to sites O2 and O3. This molecule then undergoes ionic relaxation in DFT. The ground states of the constituent atoms Mg, Si, and O are then calculated. The binding energy E_1 is given by

$$E_1 = E_T - 2E_{\text{Mg}} - E_{\text{Si}} - 4E_{\text{O}} \quad (11)$$

The calculation of λ is similar. To set up the lattice, four forsterite molecules are arranged in a supercell with an orthohombic lattice, and then relaxed in DFT as above. The energy λ is then

$$\lambda = (E_{\text{lattice}} - 4E_1)/4 \quad (12)$$

E_1	-389.6 Ry
λ (QE)	9.5
λ (ref)	7.4 [27] 9.4 [28]
λ (this work)	8.0

Table 5 E_1 and λ .

Because in the bulk silicates may be either crystalline or amorphous it would be better to use a λ reduced from the bulk crystalline to be able to explore amorphous growth. Studies of amorphous and crystalline material properties demonstrate that amorphous material has a lower bulk binding energy than the crystalline form (e.g. [25, 26]). Given the configurations of the MRO clusters in Figure 4, it is reasonable to conclude that MRO grains grow amorphously. Therefore we select value that is lower from our crystalline lattice calculation but still within the range of other studies. In the appendix we explore how different values of λ impact our results.

3. Results

3.1. Ground state configurations of $(Mg_2SiO_4)_n$ clusters

Our clusters are shown in Fig. 4. Small molecules exhibit distinct symmetries, whereas large molecules become more amorphous, but with an underlying layering of MgO and SiO₄. We find no discernible tendency towards a bulk forsterite lattice structure, and expect clusters consisting of much larger numbers of monomers are necessary for a recognizable lattice structure to form. See the work of [29, 30] for a more systematic overview of size effects in silicate dynamics.

Cohesive energies (E_b/n) are plotted in Fig. (5), along with the selected value of λ . These plots suggest convergence of these values at large monomer numbers. Edge and surface effects are still prominent in this regime (Horbach et al 1996), leading to non-monotonic growth of the cohesive energies.

3.2. Critical sizes and nucleation rates

With binding energies at hand, we can find the free energy values and determine critical sizes and nucleation rates. Fig (6) is an example of free-energy curves at selected value of saturation across a range of temperatures. At low temperature values the WCF has no maximum in the range of

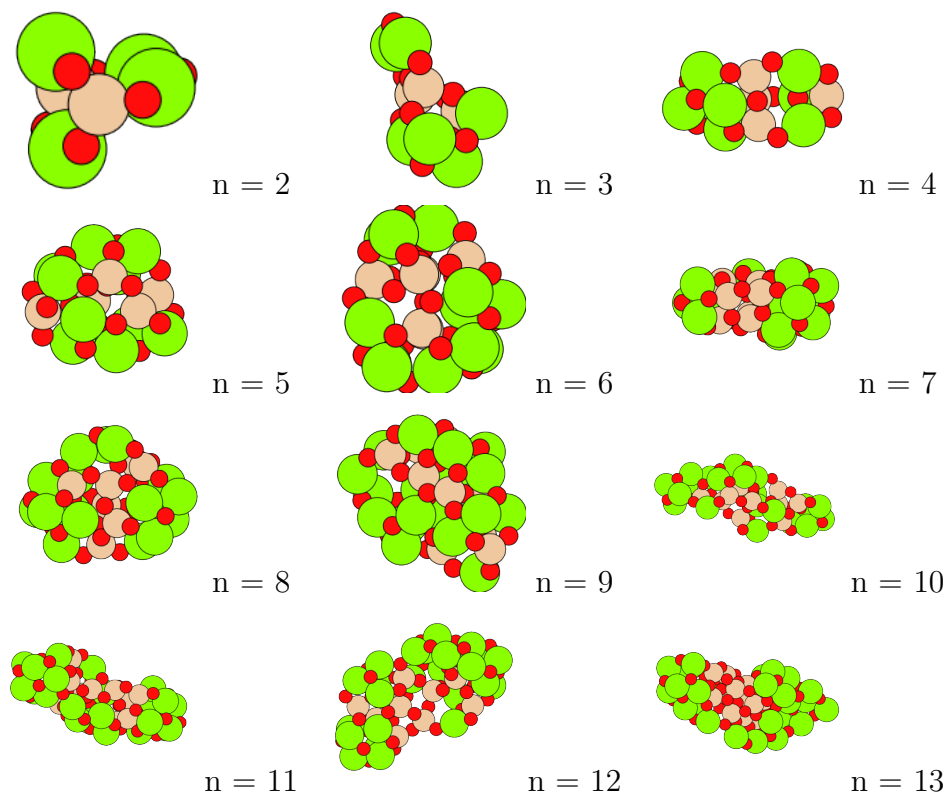


Figure 4 Clusters configurations found after DFT optimization. Colors represent atomic species: oxygen(red, small), silicon(tan, medium), magnesium(green, large).

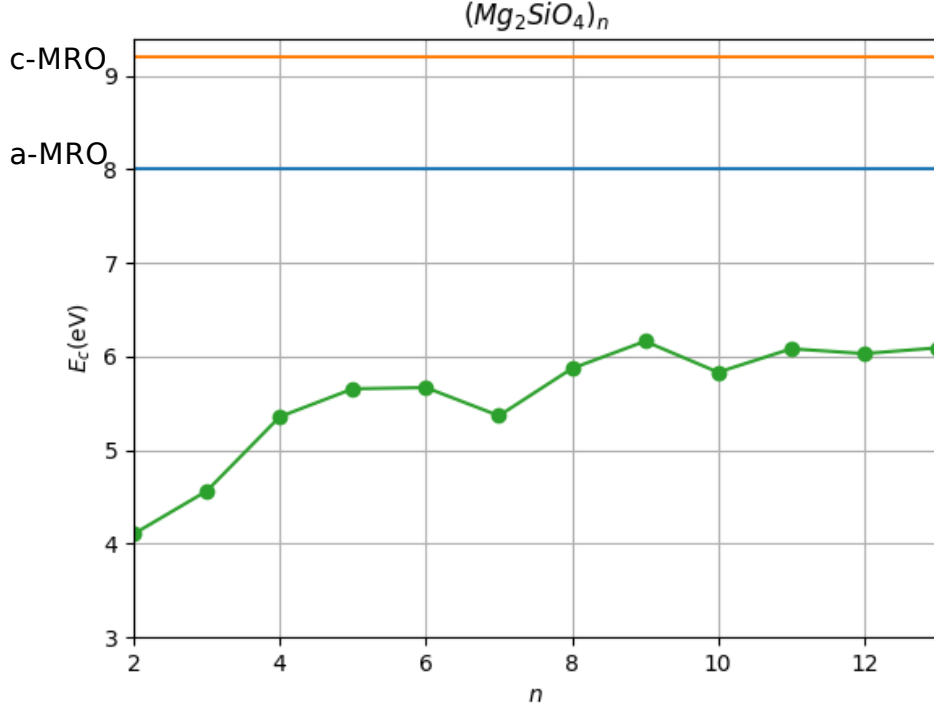


Figure 5 Cohesive energies ($=E_b/n$) of $(Mg_2SiO_4)_n$ clusters. The constant plots c-MRO and a-MRO represent the bulk cohesive energy of crystal and amorphous $(Mg_2SiO_4)_n$, respectively.

monomer numbers, indicating a critical size will be larger than the $n^* = 13$, the largest cluster we studied. For the sake of completeness we would like to investigate clusters in the regime of $n > 13$, these clusters are too large to be efficiently computed with our minima search and DFT calculations. Our size limit of $n = 13$ is equivalent to 91 atoms, already stretching the limits of our computational techniques. Physically, moreover, molecules of this size have a very slow formation rate, and their contribution to dust creation can be taken to be negligible. Conversely, at large values of (T, S) there is little to no free energy barrier and nucleation begins quickly with small clusters $n \approx 2$.

The WCF plots constructed, we can locate the maximum value and determine the critical cluster size n^* . These critical sizes across a range of

temperatures and saturations are plotted in Fig. (7), along with results from CNT for comparison. As expected $n^* = 2, 3$ for extreme environments, where density and temperature reduce the free energy barrier to the new phase and nucleation begins quickly. $n^* = 7$ is prominent in the middle regions. Comparatively colder and sparser regions of the vapor have larger free energy barriers, leading to larger critical sizes $n^* \geq 10$.

With critical sizes determined, nucleation rates follow from Eq. (10), and are plotted in Fig. (8) along with the results from CNT for comparison. Nucleation is suppressed by several magnitudes at all but the largest temperatures and saturations compared to the classical case. Our results imply that nucleation does not take place at significant rates until at least several tens of saturation. This result is consistent with the critical sizes at low saturations being very large.

4. Conclusions and Discussion

We find new results for the ground state configuration of $(\text{Mg}_2\text{SiO}_4)_n$ clusters and determine the rates of nucleation of MRO clusters in stellar outflows. Using DFT we have determined precise values of binding energies for these clusters, and used these binding energies in an atomistic formulation of nucleation theory to produce nucleation rates for silicates. These values have been compared to CNT and have been found to be significantly different than the classical case. Except for environments of large temperatures and saturations, our ANT approach finds lower formation rates of critical clusters when compared to CNT.

While we expect this trend to hold for regions of low temperature and saturations, the critical sizes that would be expected to be found at these environments are too large for our methods to efficiently determine. It is possible that at low temperatures and at saturations of approximately unity, ANT will predict enhanced nucleation over that of CNT. However, even in CNT nucleation in these environments is negligibly small (see, for instance, the low saturation regions of Figure 8).

Locating the ground state of large multi-component systems is difficult. Further limiting research into these clusters is the use of the empirical BKS model in studying nanoscale clusters. This potential form is known to perform poorly when describing the surface chemistry of silicates[31, 32]. Ideally an *ab-initio* ground-state search would be preferable. However, global minima techniques require many million energy evaluations, and at present this

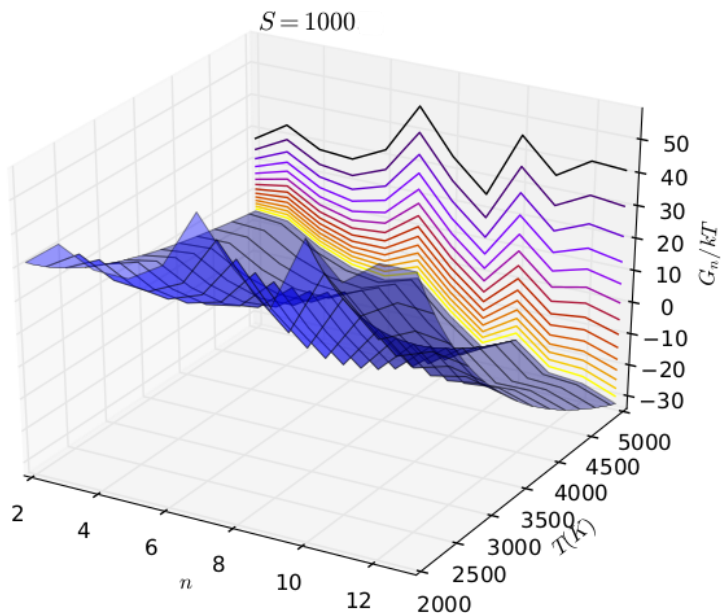


Figure 6 Work of Cluster Formation for $S = 1000$ plotted across a range of temperatures. At high temperatures the curve is flattened and critical clusters will form at small n . For lower temperatures the WCF is more jagged, leading to higher critical sizes.

approach would too computationally prohibitive.

Except for the small clusters $n = 2$, $n = 3$, and $n = 4$ the cluster configurations found do not exhibit strong symmetries or growth patterns. Larger clusters are amorphous and lack any well-structured ground state. This can be seen in the binding energy of the clusters (Figure 5), which stops growing monotonically. In the specific cases of $n = 7$ and $n = 10$ there is a significant drop in stability. While it is possible that there are configurations of clusters of comparable energies, the relative energies of the clusters will remain the same (for instance, $n = 7$ and $n = 10$ showing lowered stability.)

The drop in stability at $n = 7$ and $n = 10$ can be explained by examining the mean coordination (number of bonds) in these clusters. As seen in Figure

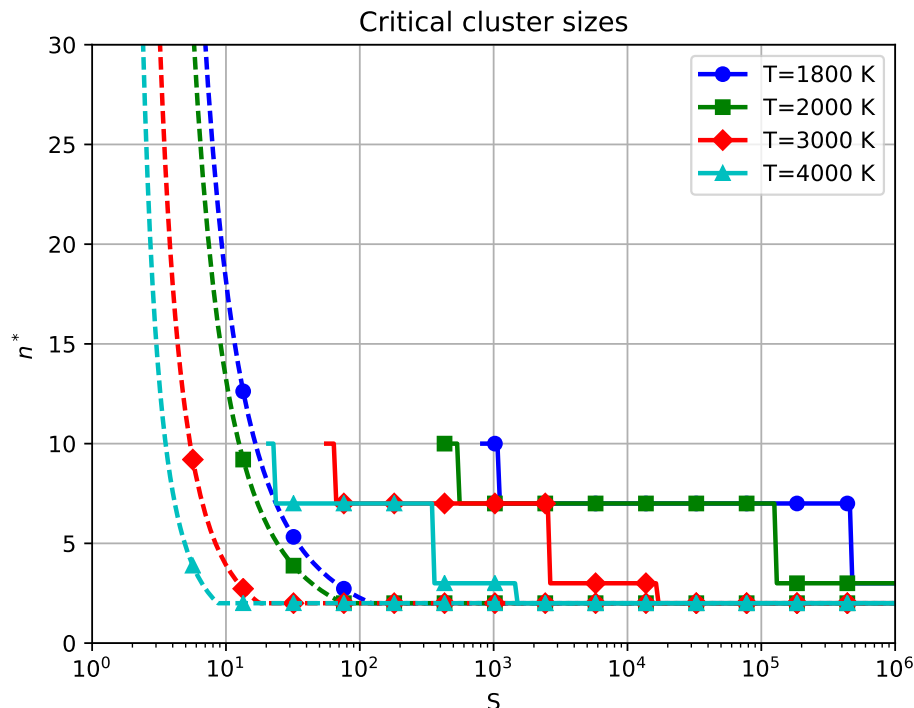


Figure 7 Critical size of $(\text{Mg}_2\text{SiO}_4)_n$ clusters as a function of saturation at constant temperatures. Dashed lines are the CNT result, solid lines are the results of this article. Note that we impose a minimum critical size of $n = 2$.

9, there is an increase in Si coordination at $n = 7$, indicating that the Si atoms are being weakly bonded to fifth O atom and weakening the stability of the SiO_4 tetrahedra. A similar, albeit smaller, effect is also noticeable at $n = 10$. It is not surprising, then, that these clusters turn out to be prominent critical sizes. Adding a monomer from the vapor to these clusters will release more free energy by lowering the mean coordination of the SiO_4 tetrahedra. At larger cluster sizes there is an overall trend in increasing Si coordination as a result of MgO-SiO_4 layering (see below).

The layering present in our results is explained by Noritake [30]. Briefly, Si-O bonds are much stronger than Mg-O bonds, leading to Si atoms preferentially sharing an oxygen bond as Si-O-Si. Thus SiO_4 tetrahedra cluster together and have overlapping O sites. These shared O atoms are not avail-

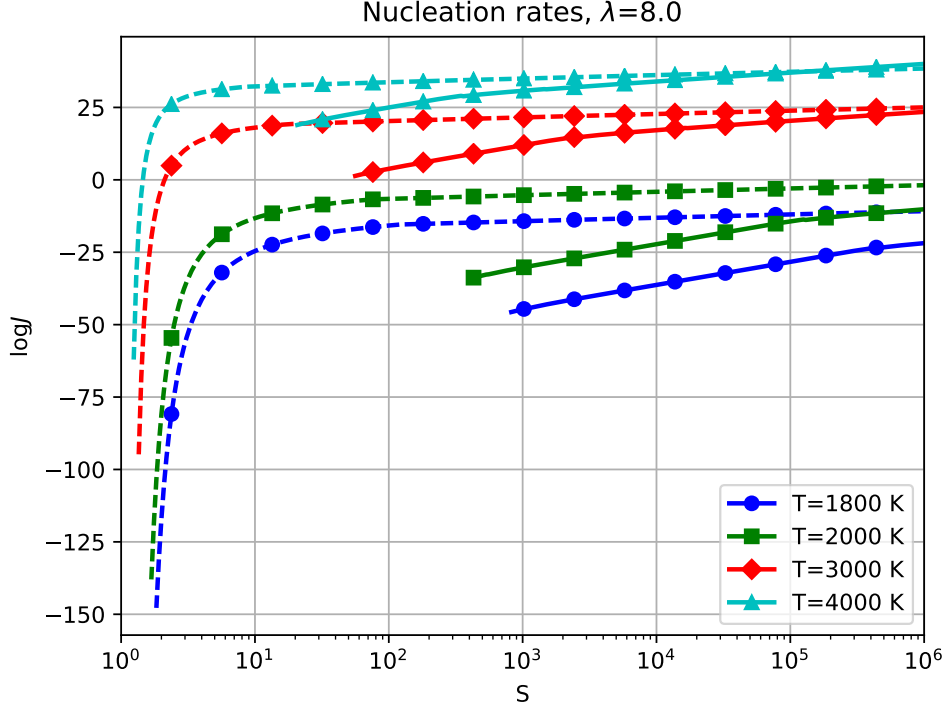


Figure 8 Nucleation rates of $(\text{Mg}_2\text{SiO}_4)_n$ clusters as a function of saturation at constant temperatures. Dashed lines are the CNT result, solid lines are the results of this article.

able to bond to Mg atoms, and the Mg will gather around excess O atoms. Our results suggest that during nucleation MROs begin as a melt, and that the emergence of Mg-Si layering explains the location of MRO critical cluster sizes.

Our results support the model that MRO dust precursor molecules form amorphyously, when following a fixed stoichiometry formation path. Evidence from simulations of silicate glasses [29] suggests that the transition from silicate melt to crystal lattice occurs in ensembles of several hundred to thousands of atoms. Crystalline silicates in late-stage stellar environments will therefore form after a period of processing and annealing. The presence of OH and Fe in the surrounding vapor will enhance the formation of crystalline MROs [33], and their inclusion in nucleation studies may result in

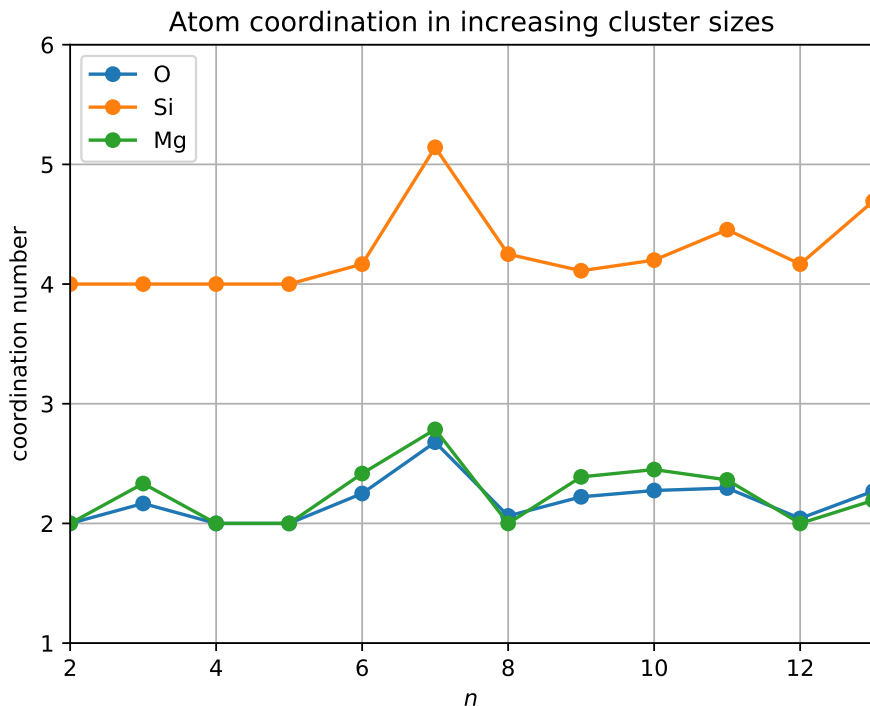


Figure 9 Average coordination of each atomic species plotted against cluster size. Increased Si coordination is seen at $n = 7$ and $n = 10$.

more crystalline-like ground states.

Critical sizes for MRO clusters are large in regions of low pressure and temperature. In Fig. 7 it can be seen that regions of low temperature and pressure show no critical size in the range of sizes we considered. In the absence of a critical size it is not possible to determine the nucleation rates in ANT. However, as can be seen in Fig. 8, nucleation rates in these regions will be near negligible, and nucleation in this regime will not be a significant contributor to dust creation. This does not mean that MRO nucleation at low temperature is impossible. Rather, the gas must achieve a very large saturation before nucleation of MRO clusters becomes efficient. At lower temperatures, nucleation of smaller silicate clusters (MgO, SiO) is more prominent [34, 12]. However, at this stage most of the condensable monomers will have nucleated into MRO clusters.

Nucleation rates are suppressed compared to CNT for all conditions save for the largest saturations we studied. In the classical theory, the value of the surface tension allows for clusters to quickly grow to the critical cluster size and begin nucleation. However, our results indicate that this value of surface tension is too low in the classical case (for instance the value given in [35] $\sigma = 425 \text{ erg cm}^{-2}$), and does not accurately represent the surface physics of nanoscale silicate clusters.

Silicate nucleation rates are suppressed at low temperatures and saturations. This suggests 'staged' nucleation periods, with carbon forming and growing quickly while silicate clusters take longer to form. Interestingly, the chemical kinetics approach reverses the priority of this staging, with carbon dust forming later than silicate clusters [36]. More detailed observations of the dust formation histories of CCNSe outflows will be useful in resolving this disagreement between models.

This work was supported in part by NSF grants 1150365-AST and 1461362-AST (DL & CM). We also would like to thank Professors Goumans and Bromley for sharing their research and providing insights into silicate cluster growth.

- [1] E. Gibb, D. Whittet, A. Boogert, A. Tielens, Interstellar ice: the infrared space observatory legacy, *The Astrophysical Journal Supplement Series* 151 (1) (2004) 35.
- [2] H. I. Teplitz, L. Armus, B. Soifer, V. Charmandaris, J. Marshall, H. Spoon, C. Lawrence, L. Hao, S. Higdon, Y. Wu, et al., Silicate emission in the spitzer irs spectrum of fsc 10214+ 4724, *The Astrophysical Journal Letters* 638 (1) (2006) L1.
- [3] P. F. Roche, C. Packham, D. K. Aitken, R. E. Mason, Silicate absorption in heavily obscured galaxy nuclei, *Monthly Notices of the Royal Astronomical Society* 375 (1) (2007) 99–104.
- [4] F. Kemper, W. Vriend, A. Tielens, The absence of crystalline silicates in the diffuse interstellar medium, *The Astrophysical Journal* 609 (2) (2004) 826.
- [5] F. Molster, L. Waters, A. Tielens, M. Barlow, Crystalline silicate dust around evolved stars-i. the sample stars, *Astronomy & Astrophysics* 382 (1) (2002) 184–221.

- [6] J. Olofsson, J.-C. Augereau, E. Van Dishoeck, B. Merín, F. Lahuis, J. Kessler-Silacci, C. Dullemond, I. Oliveira, G. Blake, A. Boogert, et al., C2d spitzer-irs spectra of disks around t tauri stars-iv. crystalline silicates, *Astronomy & Astrophysics* 507 (1) (2009) 327–345.
- [7] D. H. Wooden, D. E. Harker, C. E. Woodward, H. M. Butner, C. Koike, F. C. Witteborn, C. W. McMurtry, Silicate mineralogy of the dust in the inner coma of comet c/1995 01 (hale-bopp) pre-and postperihelion, *The Astrophysical Journal* 517 (2) (1999) 1034.
- [8] T. Henning, Cosmic silicates, *Annual Review of Astronomy and Astrophysics* 48 (2010) 21–46.
- [9] C. Mauney, M. Buongiorno Nardelli, D. Lazzati, *The Astrophysical Journal* 800 (30).
- [10] P. Todini, A. Ferrara, Dust formation in primordial Type II supernovae, *Monthly Notices of the RAS* 325 (2001) 726–736. [arXiv:astro-ph/0009176](https://arxiv.org/abs/astro-ph/0009176), [doi:10.1046/j.1365-8711.2001.04486.x](https://doi.org/10.1046/j.1365-8711.2001.04486.x).
- [11] T. Nozawa, T. Kozasa, H. Umeda, K. Maeda, K. Nomoto, Dust in the Early Universe: Dust Formation in the Ejecta of Population III Supernovae, *Astrophysical Journal* 598 (2003) 785–803. [arXiv:astro-ph/0307108](https://arxiv.org/abs/astro-ph/0307108), [doi:10.1086/379011](https://doi.org/10.1086/379011).
- [12] T. P. M. Goumans, S. T. Bromley, Efficient nucleation of stardust silicates via heteromolecular homogeneous condensation, *Monthly Notices of the RAS* 420 (2012) 3344–3349. [doi:10.1111/j.1365-2966.2011.20255.x](https://doi.org/10.1111/j.1365-2966.2011.20255.x).
- [13] S. T. Bromley, J. C. Gomez Martin, J. M. C. Plane, Under what conditions does (sio)n nucleation occur? a bottom-up kinetic modelling evaluation, *Phys. Chem. Chem. Phys.* 18 (2016) 26913–26922. [doi:10.1039/C6CP03629E](https://doi.org/10.1039/C6CP03629E).
URL <http://dx.doi.org/10.1039/C6CP03629E>
- [14] S. Goedecker, *Journal of Chemical Physics* 120 (21).
- [15] G. G. Rondina, J. L. Da Silva, Revised basin-hopping monte carlo algorithm for structure optimization of clusters and nanoparticles, *Journal of chemical information and modeling* 53 (9) (2013) 2282–2298.

- [16] B. Van Beest, G. J. Kramer, R. Van Santen, Force fields for silicas and aluminophosphates based on ab initio calculations, *Physical Review Letters* 64 (16) (1990) 1955.
- [17] A. A. Hassanali, S. J. Singer, Model for the water- amorphous silica interface: The undissociated surface, *The Journal of Physical Chemistry B* 111 (38) (2007) 11181–11193.
- [18] C. Roberts, R. L. Johnston, Investigation of the structures of mgo clusters using a genetic algorithm, *Physical Chemistry Chemical Physics* 3 (22) (2001) 5024–5034.
- [19] E. Flikkema, S. T. Bromley, A new interatomic potential for nanoscale silica, *Chemical Physics Letters* 378 (5) (2003) 622–629.
- [20] D. F. Shanno, On broyden-fletcher-goldfarb-shanno method, *Journal of Optimization Theory and Applications* 46 (1) (1985) 87–94.
- [21] D. M. Deaven, K. M. Ho, Molecular Geometry Optimization with a Genetic Algorithm, *Physical Review Letters* 75 (1995) 288–291. doi: 10.1103/PhysRevLett.75.288.
- [22] P. Giannozzi, S. Baroni, N. Bonini, M. Calandra, R. Car, C. Cavazzoni, D. Ceresoli, G. L. Chiarotti, M. Cococcioni, I. Dabo, et al., Quantum espresso: a modular and open-source software project for quantum simulations of materials, *Journal of physics: Condensed matter* 21 (39) (2009) 395502.
- [23] R. M. Martin, *Electronic Structure*, Cambridge University Press, 2004.
- [24] T. Kozasa, H. Hasegawa, Grain Formation through Nucleation Process in Astrophysical Environments. II —Nucleation and Grain Growth Accompanied by Chemical Reaction—, *Progress of Theoretical Physics* 77 (1987) 1402–1410. doi:10.1143/PTP.77.1402.
- [25] A. Thøgersen, S. Diplas, J. Mayandi, T. Finstad, A. Olsen, J. F. Watts, M. Mitome, Y. Bando, An experimental study of charge distribution in crystalline and amorphous si nanoclusters in thin silica films, *Journal of Applied Physics* 103 (2) (2008) 024308.

- [26] W. Gonçalves, J. Morthomas, P. Chantrenne, M. Perez, G. Foray, C. L. Martin, Molecular dynamics simulations of amorphous silica surface properties with truncated coulomb interactions, *Journal of Non-Crystalline Solids* 447 (2016) 1–8.
- [27] M. Catti, The lattice energy of forsterite. Charge distribution and formation enthalpy of the $\text{SiO}\{_4/4^{-}\}$ ion, *Physics and Chemistry of Minerals* 7 (1981) 20–25. doi:10.1007/BF00308196.
- [28] P. W. May, G. Pineau des Forêts, D. R. Flower, D. Field, N. L. Allan, J. A. Purton, Sputtering of grains in C-type shocks, *Monthly Notices of the RAS* 318 (2000) 809–816. doi:10.1046/j.1365-8711.2000.03796.x.
- [29] J. Horbach, W. Kob, K. Binder, C. A. Angell, Finite size effects in simulations of glass dynamics, *Physical Review E* 54 (1996) R5897–R5900. arXiv:cond-mat/9610066, doi:10.1103/PhysRevE.54.R5897.
- [30] F. Noritake, K. Kawamura, Structure and properties of forsterite-MgSiO₃ liquid interface: molecular dynamics study, *Progress in Earth and Planetary Science* 1 (2014) 14. doi:10.1186/2197-4284-1-14.
- [31] D. Ceresoli, M. Bernasconi, S. Iarlori, M. Parrinello, E. Tosatti, Two-membered silicon rings on the dehydroxylated surface of silica, *Physical review letters* 84 (17) (2000) 3887.
- [32] E. Flikkema, S. Bromley, *Chemical Physics Letters* 378 (5).
- [33] C. Jäger, F. Molster, J. Dorschner, T. Henning, H. Mutschke, L. Waters, Steps toward interstellar silicate mineralogy. iv. the crystalline revolution, *Astronomy and Astrophysics* 339 (1998) 904–916.
- [34] K. S. Jeong, J. M. Winters, T. Le Bertre, E. Sedlmayr, Self-consistent modeling of the outflow from the O-rich Mira IRC -20197, *Astronomy and Astrophysics* 407 (2003) 191–206. doi:10.1051/0004-6361:20030693.
- [35] R. E. Boni, G. Derge, Surface Tensions of Silicates, *JOM - Journal of the Minerals, Metals and Materials Society* 8 (1956) 53–59. doi:10.1007/BF03377643.
- [36] A. Sarangi, I. Cherchneff, *Astronomy and Astrophysics* 575 (A95).

Appendix A. Effect of λ values on nucleation rates

The parameter λ represents the work required to remove a monomer from the bulk solid phase. This value is used in the atomistic formulation of nucleation rates to determine the surface energy of a cluster, as in Eq. (8). The complex nature of amorphous silicate growth prevents simple evaluation of this parameter. In section 2 we present our approach to selection of this value for this work. In this appendix we present results of nucleation rates with lower and higher values of λ .

Lower values of λ imply a lower energy barrier between phases, and this will induce faster nucleation. This can be seen in Fig. A.10. Nucleation rates are still suppressed compared to classical nucleation, but lower saturations are required to begin nucleation. This corresponds physically to a mostly free formation pathway. While our results indicate that silicate growth is amorphous, there is indeed some underlying constraints on growth (for instance, the MgO-SiO₄ layering) that would argue against using such a low value for λ .

Fig. A.11 represents a larger value of λ , and shows significantly less nucleation. This corresponds to a much more constrained formation pathway, i.e. crystal growth. As we do not see evidence of crystal structure in our low-lying cluster configurations, it seems unlikely that such a large value of λ is applicable to astrophysical dust nucleation.

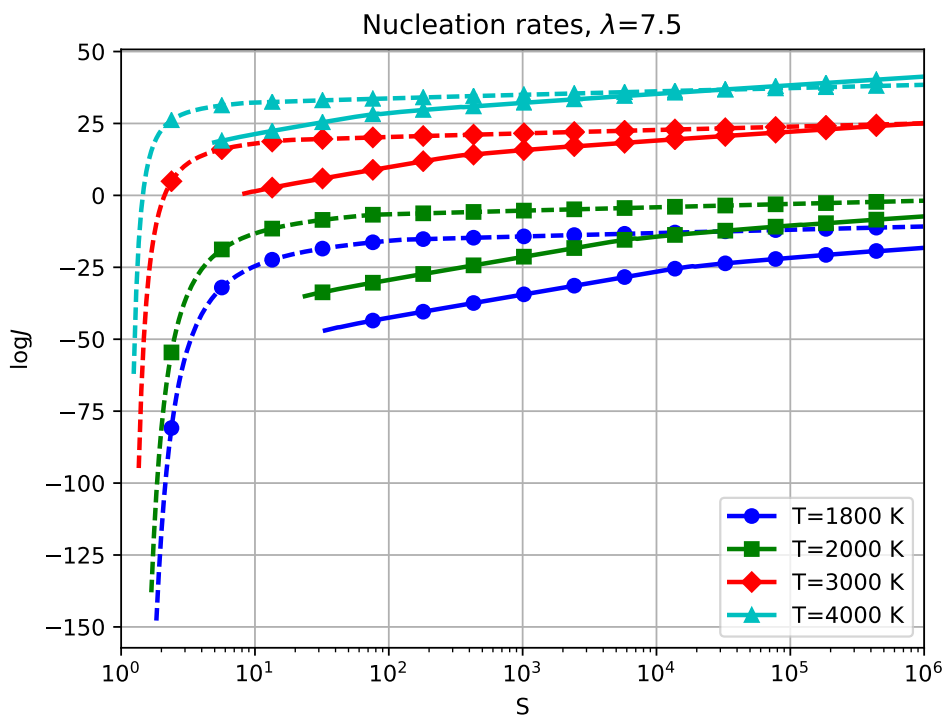


Figure A.10 Nucleation rates at $\lambda = 7.5$ eV. Dashed lines are the CNT result, solid lines are the results of this article. Temperatures given in Kelvins.

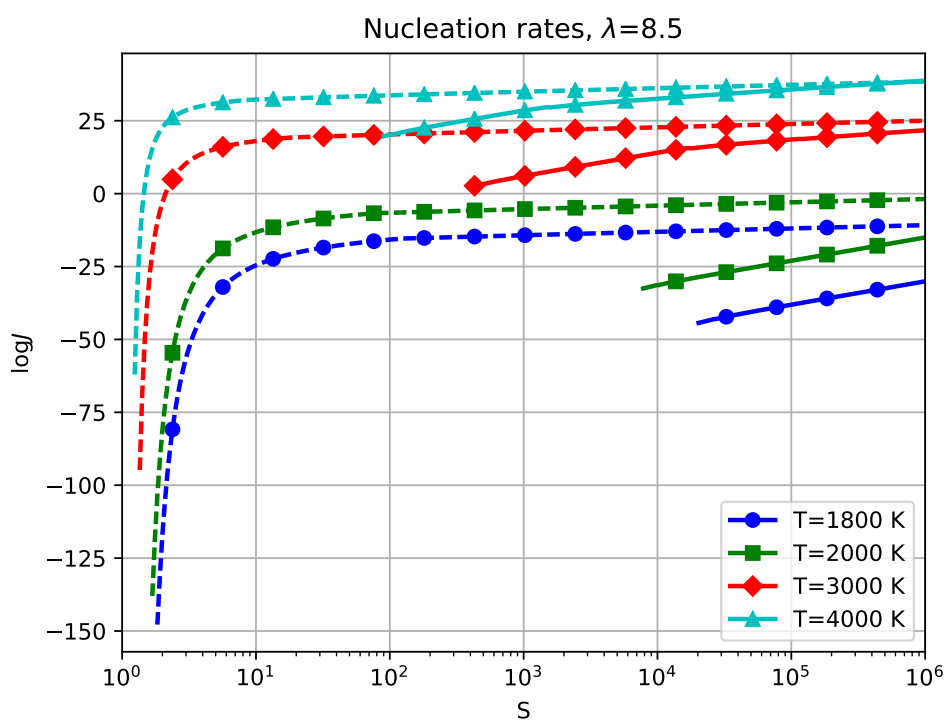


Figure A.11 Nucleation rates at $\lambda = 8.5$ eV. Dashed lines are the CNT result, solid lines are the results of this article. Temperatures given in Kelvins.